

Accelerate 3D Object Detection Models via Zero-Shot Attention Key Pruning

Lizhen Xu¹, Xiuxiu Bai¹, Xiaojun Jia², Jianwu Fang¹, Shanmin Pang¹

¹Xi'an Jiaotong University, ²Nanyang Technological University

Abstract

Query-based methods with dense features have demonstrated remarkable success in 3D object detection tasks. However, the computational demands of these models, particularly with large image sizes and multiple transformer layers, pose significant challenges for efficient running on edge devices. Existing pruning and distillation methods either need retraining or are designed for ViT models, which are hard to migrate to 3D detectors. To address this issue, we propose a zero-shot runtime pruning method for transformer decoders in 3D object detection models. The method, termed **tgGBC** (trim keys gradually **G**uided By **C**lassification scores), systematically trims keys in transformer modules based on their importance. We expand the classification score to multiply it with the attention map to get the importance score of each key and then prune certain keys after each transformer layer according to their importance scores. Our method achieves a 1.99x speedup in the transformer decoder of the latest ToC3D model, with only a minimal performance loss of less than 1%. Interestingly, for certain models, our method even enhances their performance. Moreover, we deploy 3D detectors with tgGBC on an edge device, further validating the effectiveness of our method. The code can be found at https://github.com/iseri27/tg_gbc.

1. Introduction

Vision-based 3D object detection is a crucial technique that empowers intelligent devices to perceive and interpret the real world precisely. In recent years, query-based models [5, 14, 19, 20, 22, 24, 25, 32–35, 37, 40] have risen to prominence as the state-of-the-art paradigm in the field of 3D object detection. These methodologies typically employ a CNN or ViT backbone [7, 9, 12, 18] for image feature extraction, followed by sophisticated processing through a multi-layer transformer decoder. Based on their distinct approaches to feature map processing and attention mechanism implementation, these methods can be fundamentally classified into two categories: **dense methods** and **sparse methods**. Dense methods facilitate com-

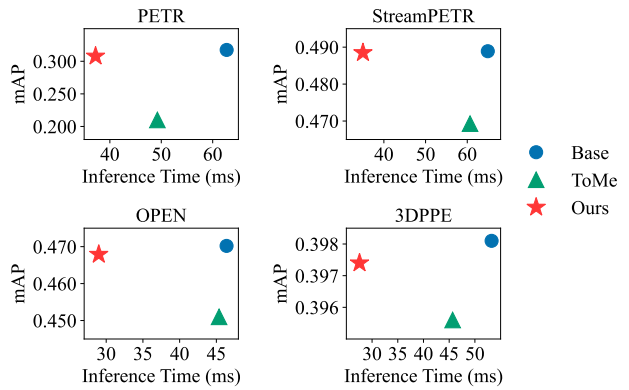


Figure 1. The mAP and inference time of models, comparing with applying tgGBC and ToMe [1].

prehensive global interactions across entire feature maps [14, 24, 25, 28, 32, 33], enabling holistic information integration. In contrast, sparse methods accelerate model convergence by focusing on a carefully selected subset of feature maps [15, 20, 23, 34, 37], often leveraging deformable attention mechanisms [41] to improve computational efficiency. Despite significant progress in sparse methodologies, dense methods continue to play a pivotal role in 3D object detection, largely attributed to their superior detection accuracy (see detailed discussion in Appendix A.2). The sustained importance of dense approaches is further strengthened through ongoing advancements, where researchers are actively proposing and implementing novel methodologies and architectural refinements [14, 40].

Nevertheless, dense methods also present a notable limitation: their characteristic global feature interactions incur substantial computational overhead, requiring dedicated optimization strategies like pruning [6, 8, 11, 26, 27, 38] or distillation [4, 13, 21] for effective deployment on resource-constrained edge platforms. In this context, retraining-free pruning approaches have recently emerged as a promising research direction, attracting considerable attention from the community [1, 10, 16, 17, 31, 39]. Based on the phase in which pruning methods are applied, they can be broadly categorized into two distinct types: **static pruning** and **runtime pruning**. Static pruning methods [16, 17] typically operate by executing the model on a small-scale subset of

data to identify and preserve critical parameters. While these approaches effectively reduce both model parameters and GPU memory consumption during runtime, they inherently require model execution to conduct the parameter search. The efficiency and efficacy of static pruning are influenced by several factors, including the model’s architectural complexity, its scale, and the representativeness of the subset data used for pruning. Moreover, each static pruning method is specifically designed for a particular model or class of methods. Therefore, static pruning methods designed for image classification tasks[16] cannot be directly transferred to 3D detection tasks, limiting their universality.

Runtime pruning methods integrate pruning layers between specific model modules without altering the original model parameters, thereby enabling dynamic pruning during inference [1, 10, 31]. This approach provides a plug-and-play solution that incurs no additional training costs while significantly accelerating model inference, making it a zero-overhead optimization strategy. Unlike static pruning, runtime pruning eliminates the need for retraining, parameter search, or reliance on a sub-dataset. Users only need to integrate the pruning layer into the model and execute the inference procedure as usual.

To accelerate model inference speed without retraining, we propose tgGBC, a runtime pruning method that progressively removes keys from transformer modules based on their importance. 3D object detectors usually adopt stacked transformer layers, each comprising a self-attention and a cross-attention module. During inference, these detectors determine which predictions to retain based on the classification scores, as higher scores indicate more accurate bounding boxes and attributes. We integrate our tgGBC module between two transformer layers to reduce the number of keys. This module takes as input the classification scores from a CNN head and the attention map produced by the cross-attention module. By multiplying the classification scores with the attention map and then computing their sum, we transfer the quality of the classification scores to each key. The least important r keys are then pruned, significantly optimizing computation. As shown in Fig. 1, integrating tgGBC into popular 3D detection models results in nearly a $2\times$ speedup in transformer decoder inference while incurring only a minimal drop in mAP.

To summarize, our contributions are as follows:

- We propose tgGBC, a zero-shot pruning technique that accelerates dense transformer decoders in 3D object detectors. To the best of our knowledge, this is the first work to explore zero-shot, retraining-free pruning for 3D object detection models.
- We calculate the importance of each key using the classification scores and attention maps that are inherently generated within the transformer decoder without introducing any additional parameters.

- Extensive experimental results show that tgGBC accelerates the transformer decoder of dense 3D detectors by nearly $2\times$ with minimal performance degradation. Furthermore, when deploying FocalPETR [32] and Stream-PETR [33] on an edge device with tgGBC, we respectively achieve $1.18\times$ and $1.19\times$ speedup in inference, demonstrating its efficiency in real-world scenarios.

2. Related Works

2.1. Query-based 3D Object Detection Methods

Transformer [30], as a prominent attention mechanism, has been extensively adopted in object detection tasks. DETR [3] is the first model to successfully integrate transformer architecture into 2D object detection, utilizing learnable queries for object prediction. Building upon this framework, the query-based paradigm has demonstrated remarkable success in advancing 3D object detection methodologies. PETR [24] generates position-aware 3D features to help detect objects. FocalPETR [32] uses a 2D auxiliary task to select more confident priors. 3DPPE [28] introduces 3D point positional encoding by using a depth predictor. OPEN [14] proposes an object-wise position embedding to inject object-wise depth information into the network. M-BEV [5] introduces a generic masked BEV perception framework designed to handle situations where one or more cameras fail, which enhances the safety and robustness of perception algorithms. ToC3D [40] proposes a token compression backbone to speed up the model’s inference.

Despite their varying architectural designs, the aforementioned 3D object detection methods maintain a consistent framework characterized by an image backbone coupled with a multi-layer transformer decoder.

2.2. Retraining-free Pruning for Transformers

Retraining-free pruning methodologies have recently gained significant attention in the research community. Among these, static pruning techniques [16, 17] have shown particular promise by enabling model optimization before deployment, typically utilizing small-scale datasets for parameter adjustment.

In parallel development, runtime pruning approaches insert a pruning layer inside the model. ATS [10] uses classification tokens—a special structure in ViT models—as pruning criterion. ToMe [1] divides tokens into two groups and uses a bipartite matching algorithm to pair them one-to-one, merging the top- r pairs with the highest r similarity. Notably, Zero-TPrune [31] employs an extended Markov algorithm, treating the attention map as the state transition matrix of a Markov chain and using the converged state as the pruning criterion for tokens.

However, these methods face significant challenges when adapted to 3D detection tasks. In query-based 3D

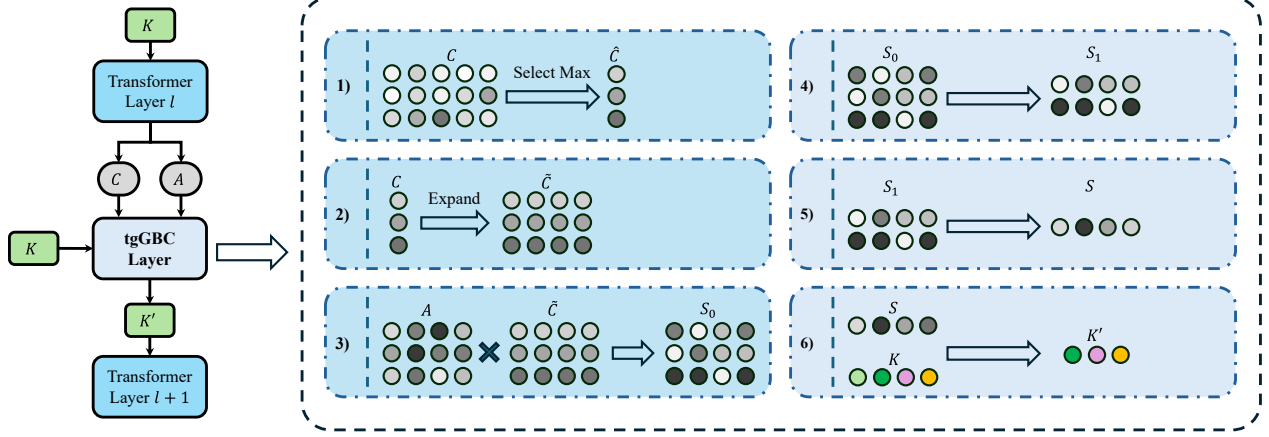


Figure 2. TgGBC layer is inserted after the first n transformer decoder layers, taking classification scores C , attention weights A and keys K as input. Inside the tgGBC layer, 1) we select the maximum of each classification vector, resulting in $\hat{C} \in \mathbb{R}^{N_q}$; 2) repeat and expand \hat{C} to a shape of $\mathbb{R}^{N_q \times N_k}$, got \tilde{C} ; 3) calculate $S_0 = A \odot \tilde{C} \in \mathbb{R}^{N_q \times N_k}$; 4) select k lines of S_0 with highest k classification scores, got S_1 ; 5) conduct sum of S_1 along column, got key importance S ; 6) prune r keys with the lowest importance value.

detection models, the use of panoramic cameras and high-resolution image inputs leads to a substantial increase in token number compared to ViT-based models. For instance, while ViT-based models [7, 9, 29] typically process 1,024 tokens at a resolution of 448×448 , 3D object detection models must handle a significantly larger token space—4,224 tokens even at a minimal resolution of 704×256 . This dramatic increase in token count severely impacts the computational efficiency of methods like ToMe, which relies on similarity matrix calculations with quadratic time complexity. Additionally, Zero-TPrune’s architectural design, though effective for ViT models, is fundamentally limited by its dependence on square attention matrices. In ViT architectures, tokens simultaneously serve as *query*, *key*, and *value* within attention modules. In contrast, 3D object detection models utilize distinct *query* and *key*, resulting in the generation of non-square attention maps, making it impossible to adapt Zero-TPrune to 3D detectors.

To address these challenges, we introduce a runtime pruning module optimized for 3D object detection tasks.

3. Method

3.1. Preliminary and Feasibility

Before delving into our approach, it is essential to understand why pruning keys is feasible.

Consider a multi-head attention mechanism with N_h heads and an embedding dimension of E . A key requirement is that E must be an integer multiple of N_h to ensure that the embedding can be evenly partitioned across all attention heads. We define the dimensionality of each attention head as $E_h = E/N_h$. The multi-head attention mechanism begins by projecting the input queries, keys, and values using learnable parameter matrices $W^Q, W^K, W^V \in \mathbb{R}^{E \times E}$,

$\mathbb{R}^{E \times E}$, formulated as:

$$Q \leftarrow QW^Q, \quad K \leftarrow KW^K, \quad V \leftarrow VW^V \quad (1)$$

where $Q \in \mathbb{R}^{N_q \times E}$, $K, V \in \mathbb{R}^{N_k \times E}$ represent *query*, *key* and *value* matrices respectively.

To enable multi-head attention, the projected matrices Q is split along the embedding dimension to obtain head-specific representations q^h :

$$q^h = Q_{:,h \times E_h:(h+1) \times E_h} \in \mathbb{R}^{N_q \times E_h} \quad (2)$$

k^h and v^h are obtained similarly. For each attention head h , the attention map matrix A^h is computed using the scaled dot product:

$$A^h = \text{Softmax} \left(\frac{q^h \times (k^h)^T}{\sqrt{E}} \right) \in \mathbb{R}^{N_q \times N_k} \quad (3)$$

The attention map A^h is then multiplied by v^h to obtain the head-specific output O^h : $O^h = A^h \times v^h \in \mathbb{R}^{N_q \times E_h}$. The final output $O \in \mathbb{R}^{N_q \times E}$ of the attention module is obtained by concatenating the outputs from all attention heads:

$$O = \text{Concat}_{h \in \{1, \dots, N_h\}} (O^h) \times W^O, O \in \mathbb{R}^{N_q \times E} \quad (4)$$

where $W^O \in \mathbb{R}^{E \times E}$ is a learnable parameter.

As shown in Figure 8 (in Appendix A.1), 3D detectors typically include both self-attention and cross-attention modules within each transformer layer. The self-attention module takes pre-defined queries as Q , K and V , and its output is then used as Q in the subsequent cross-attention module. Notably, in 3D object detection models, V is always identical to K .

From Eq. (1)-Eq. (4), we observe that the shape of the attention output is independent of N_k . Therefore, for an attention module with learnable parameters $W^Q, W^K, W^V, W^O \in \mathbb{R}^{E \times E}$, the original parameters remain valid even when modifying N_q and N_k , as long as the following two conditions are met: 1) the embedding dimension E remains unchanged to match the projection parameters W^Q, W^K, W^V and W^O ; 2) the number of keys and values remains equal.

Thus, it is feasible to dynamically prune keys in dense models with global attention during runtime without modifying the model parameters. However, it should be noted that key pruning may not be applicable to models utilizing sparse attention mechanisms, such as deformable attention or flash attention, since these approaches inherently lack an attention map [15, 22, 23, 34, 41].

3.2. Pruning Criterion

As highlighted in GPQ [36], predictions with the highest classification scores are retained as final outputs. Consequently, keys that contribute minimally to these high-confidence predictions can be considered unimportant and pruned without significantly affecting the final results.

According to Eq. (1)-Eq. (4), it is clear that the number of final predictions is determined by the number of queries N_q rather than the number of keys N_k . This implies that pruning should first target unimportant queries—those whose predictions are less likely to be selected in the final results. Fortunately, query importance can be directly assessed using classification scores [36].

Once unimportant queries are identified, the next step is to find which keys are most relevant to them. The attention map entry $A_{i,j}$ directly represents the correlation between query q_i and key k_j . Thus, a natural pruning criterion is to compute the importance of each key as the sum of the product of classification scores and attention weights. Keys with the lowest importance values can then be pruned, reducing computational cost while preserving model performance.

3.3. Pruning Process

The pruning process is illustrated in Fig. 2. Before pruning, we first need to obtain classification scores $C \in \mathbb{R}^{N_q \times N_C}$ and attention weights $\{A^h\}$ from the previous transformer decoder layer, where N_C represents the number of object classes to be predicted. TgGBC begins by selecting the maximum value from each classification vector C_i , yielding $\hat{C} \in \mathbb{R}^{N_q}$:

$$\hat{C}_i = \max_j C_{i,j}, \forall i \in \{1, 2, \dots, N_q\} \quad (5)$$

Then, \hat{C} is repeated N_k times, resulting in the expanded classification scores $\tilde{C} \in \mathbb{R}^{N_q \times N_k}$:

$$\tilde{C}_{i,m} = \hat{C}_i, \forall m \in \{1, \dots, N_k\} \quad (6)$$

Next, we conduct element-wise multiplication between the averaged attention map A and the expanded classification scores \tilde{C} :

$$S_0 = A \odot \tilde{C}, \quad A = \frac{1}{N_h} \sum_{i=1}^h A_i \quad (7)$$

where $S_0 \in \mathbb{R}^{N_q \times N_k}$, its i -th row, $(S_0)_i$, corresponds to the classification score \hat{C}_i . We then select the top- k rows with the highest classification scores, obtaining $S_1 \in \mathbb{R}^{k \times N_k}$:

$$S_1 = (S_0)_{\Phi}, \quad \Phi = \{i \mid \max_j C_{i,j} \geq c_k\} \quad (8)$$

where c_k represents the k -th largest value in \hat{C} .

Finally, we compute the sum along the columns of S_1 , yielding the token importance scores $S \in \mathbb{R}^{N_k}$:

$$S_j = \sum_{i=1}^k (S_1)_{i,j} \quad (9)$$

Once the importance scores S are obtained, we prune the keys with the lowest importance values.

Assuming the transformer decoder has L layers and takes N_k keys as input, our goal is to prune a total of r keys. To achieve this, we remove $\lfloor \frac{r}{n} \rfloor$ keys per layer, where $1 \leq n \leq N_k - 1$. Unlike ToMe, which relies on bipartite matching, our approach allows pruning all r keys within a single layer, even when r is close to 90% of N_k .

The analysis of the cost of tgGBC can be found in Appendix B.

4. Experiments

4.1. Experimental Setup

Our experiments are conducted on the nuScenes [2] dataset, and we use evaluation metrics established by this dataset. The primary evaluation metric is mean Average Precision (mAP), which serves as the fundamental measure of detection accuracy. In addition to spatial localization, 3D object detection requires precise prediction of object characteristics, including orientation, velocity, and specific attributes. To comprehensively assess these capabilities, nuScenes introduces five complementary metrics collectively referred to as mTP: mean Average Translation Error (mATE), mean Average Scale Error (mASE), mean Average Orientation Error (mAOE), mean Average Velocity Error (mAVE), and mean Average Attribute Error (mAAE).

To offer a holistic evaluation framework, nuScenes proposes the nuScenes Detection Score (NDS), providing a comprehensive assessment of model performance across all critical detection aspects. The NDS is computed using the formula: $NDS = \frac{1}{5} \left[5mAP + \sum_{mTP} (1 - \min(1, mTP)) \right]$, where $mTP \in \{mATE, mASE, mAOE, mAVE, mAAE\}$.

Model	Backbone	ImageSize	N_k	r	mAP \uparrow	NDS \uparrow	mATE \downarrow	mASE \downarrow	mAOE \downarrow	mAVE \downarrow	mAAE \downarrow	Inf. Time (ms) \downarrow	Dec. Time (ms) \downarrow
PETR [24] (ECCV 2022)	ResNet50	1408x512	16896	-	31.74% 0.3669		0.8392 0.2797	0.6145 0.9521	0.2322		131.94	47.09	
	VovNet	1600x640	24000	12000	30.78% 0.3579		0.8540 0.2832	0.6168 0.9703	0.2354		112.88(-14.45%)	28.58(-39.31%)	
FocalPETR [32] (IEEE TIV 2023)	ResNet18	1408x512	16896	-	40.45% 0.4517		0.7287 0.2706	0.4485 0.8399	0.2178		281.05	62.72	
	VovNet	800x320	6000	3000	39.53% 0.4432		0.7482 0.2720	0.4538 0.8539	0.2167		254.18(-9.56%)	37.22(-40.66%)	
StreamPETR [33] (ICCV 2023)	ResNet50	704x256	4224	-	32.24% 0.3566		0.7684 0.2803	0.6530 1.0942	0.3447		80.87	44.26	
	VovNet	1600x640	24000	2000	31.70% 0.3530		0.7767 0.2806	0.6503 1.0935	0.3466		62.10(-23.21%)	26.01(-41.23%)	
3DPPE [28] (ICCV 2023)	VovNet	800x320	6000	-	42.36% 0.4716		0.6572 0.2658	0.4582 0.8050	0.2159		99.14	24.65	
	VovNet	800x320	3000		42.38% 0.4719		0.6560 0.2663	0.4572 0.8045	0.2157		89.66(-9.56%)	17.08(-30.71%)	
MV2D [35] (ICCV 2023)	ResNet50	1408x512	-	-	44.92% 0.5399		0.6246 0.2657	0.3840 0.4009	0.1722		416.61	96.58	
	VovNet	1408x512	-	50%	44.11% 0.5384		0.6248 0.2657	0.3844 0.4024	0.1717		388.58(-6.73%)	70.83(-26.66%)	
M-BEV [5] (AAAI 2024)	VovNet	800x320	12000	-	35.14% 0.4640		0.7300 0.2717	0.4980 0.4324	0.1845		178.87	55.14	
	VovNet	800x320	6000		34.37% 0.4557		0.7520 0.2744	0.5099 0.4376	0.1872		151.00(-15.58%)	33.96(-38.41%)	
OPEN [14] (ECCV 2024)	ResNet50	704x256	4224	-	47.02% 0.5657		0.5676 0.2702	0.4221 0.2321	0.2019		77.25	33.63	
	VovNet	800x320	6000	-	46.85% 0.5637		0.5682 0.2705	0.4311 0.2325	0.2031		65.18(-15.62%)	24.23(-27.95%)	
	ResNet101	1408x512	16896	12000	52.07% 0.6128		0.5250 0.2566	0.2811 0.2148	0.1982		118.55	29.35	
ToC3D [40] (ECCV 2024)	ToC3DViT	1600x800	30000	-	52.09% 0.6129		0.5249 0.2569	0.2808 0.2146	0.1986		111.40(-6.03%)	23.26(-20.75%)	
	ToC3DViT	1600x800	27000		51.80% 0.6043		0.5314 0.2679	0.3457 0.2095	0.1922		196.55	46.39	
	ToC3DViT	1600x800	30000	27000	51.57% 0.6019		0.5368 0.2726	0.3493 0.2102	0.1905		178.35(-9.31%)	28.99(-37.51%)	
	ToC3DViT	1600x800	30000	27000	54.20% 0.6187		0.5589 0.2571	0.2716 0.2353	0.2007		863.47	77.92	
	ToC3DViT	1600x800	30000	27000	53.43% 0.6113		0.5842 0.2589	0.2744 0.2370	0.2038		817.69(-5.30%)	39.17(-49.73%)	

Table 1. Pruning results for different models. Results shown in the table all use a setting of $n = 2$ and $k = 175$ when tgGBC is applied. The column “ N_k ” indicates the number of keys. We report inference time of the whole model as shown in column “Inf. Time” and the time of the transformer decoder only as shown in the column “Dec. Time”. The speed is tested on a single RTX3090. Due to MV2D’s special design, its number of keys is floating, hence, we prune 50% of keys according to the current number of keys.

To validate the effectiveness and efficiency of tgGBC, we perform experiments on eight 3D advanced detectors: PETR [24], FocalPETR [32], StreamPETR [33], OPEN [14], ToC3D [40], 3DPPE [28], MV2D [35] and M-BEV [5]. All experiments are conducted under their original configurations to ensure fair and consistent comparisons.

4.2. Effectiveness Assessment

The primary challenge for retraining-free pruning methods is maintaining model performance while improving efficiency. Tab. 1 reports the performance and inference time of various models after pruning about 50%-90% of keys. The maximum number of keys that can be pruned varies across different models. To ensure a fair and clear comparison, we use a standardized experimental setup of $n = 2$ and $k = 175$. While these results may not represent the optimal configurations for every model, they provide a clear evaluation of the effectiveness of tgGBC.

For 3DPPE with VovNet as the backbone and an image size of 800×320 , pruning 3000 keys (50% of the original 6000 keys) results in an mAP of 39.74%, with only a 0.07% drop. Meanwhile, inference time saves by 22.76% ($1.29 \times$ faster) for the whole model and 48.24% ($1.93 \times$ faster) for the transformer decoder. Interestingly, for certain models such as FocalPETR-vov-800x320 and OPEN-vov-800x320, applying tgGBC leads to a slight increase in mAP, suggest-

ing potential benefits beyond just efficiency improvements.

For models with large image sizes, such as StreamPETR-vov-1600x640, tgGBC successfully prunes 21,000 out of 24,000 keys (87.5%), resulting in an 11.57% reduction in overall inference time ($1.13 \times$ faster) and a 46.13% reduction in decoder time ($1.86 \times$ faster). The speedup achieved by tgGBC varies depending on the backbone size of the model. Even for ToC3D, which features a super large backbone and high-resolution images (1600×800), tgGBC still reduces overall inference time by 5.30%, while the decoder time decreases by 49.73% ($1.99 \times$ faster)—all without compromising model performance.

NDS, which reflects the overall performance of the model, remains highly stable with tgGBC, maintaining a drop within 1%. For instance, when applying tgGBC to OPEN-ResNet50-704x256, the NDS decreases by only 0.002, demonstrating minimal impact on performance. Interestingly, some mTPs (mean True Positives) have even decreased after applying tgGBC. For example, the mAAE of MV2D decreases from 0.1722 to 0.1717, as shown in Tab. 1. For optimal and more comprehensive results with different configurations, please refer to Appendix C.1.

In addition to quantitative results, we provide visualizations of PETR [24], FocalPETR [32], StreamPETR [33], OPEN [14], 3DPPE [28] and ToC3D [40] in Fig. 3. These visualizations demonstrate that bounding boxes remain

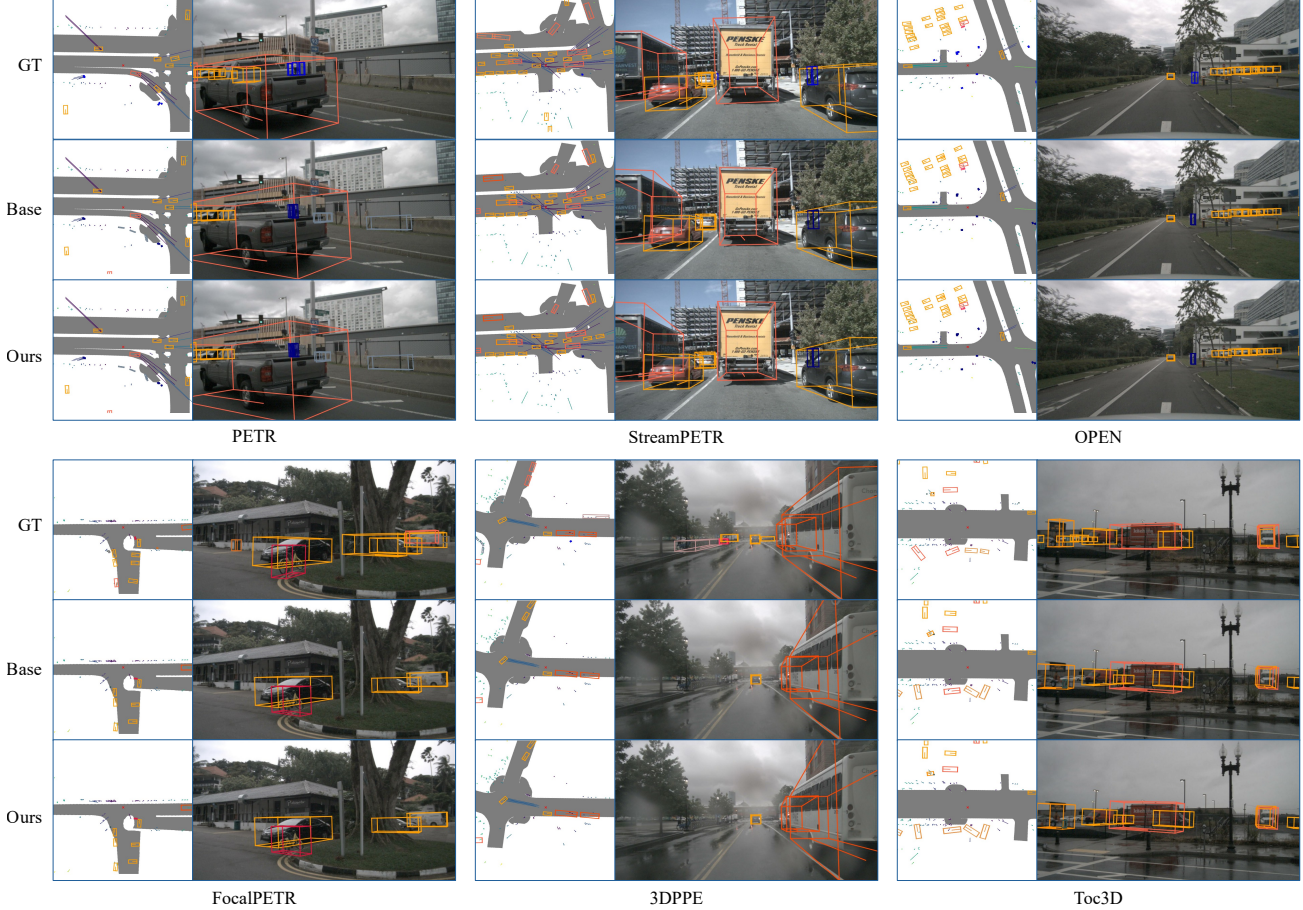


Figure 3. Visualization results for different models with top-down view(left for each sub-figure) and camera view.

largely unchanged after applying tgGBC, further validating its effectiveness.

4.3. Comparison with ToMe

As the first method to explore zero-shot, retraining-free pruning for 3D object models, there are no directly comparable methods in the literature. To validate the effectiveness of our approach, we benchmark tgGBC against ToMe, an advanced runtime pruning technique designed to accelerate ViT-based models. While ToMe is primarily designed for 2D vision tasks, it represents the closest existing work in terms of runtime pruning efficiency, making it a relevant baseline for comparison. This allows us to demonstrate the advantages of tgGBC in optimizing 3D models.

As shown in Tab. 2, ToMe significantly degrades the performance of both StreamPETR and OPEN while offering limited improvements in inference speed. In some cases, such as OPEN with VovNet, the computational overhead of calculating the similarity matrix outweighs the benefits, resulting in a slowdown rather than an acceleration.

For further comparisons with more models across different values of r and n , please refer to Appendix C.2.

4.4. Inference Speed on OrangePi

A major challenge in deploying models for real-world applications is achieving efficient inference on edge devices. To evaluate the impact of tgGBC on edge-device performance, we deployed FocalPETR and StreamPETR on OrangePi. As shown in Tab. 3, tgGBC improves inference efficiency. For FocalPETR-r18-1408x512, tgGBC reduces inference time by 15.47%, making the model 1.18 \times faster. For StreamPETR-vov-1600x640, tgGBC achieves a 16.11% reduction in inference time, speeding up the model by 1.19 \times .

Meanwhile, quantization is also a common method for accelerating model inference. We quantized the model to fp16 format and compared it with the non-quantized version. The results, shown in Tab. 3, confirm that our method can still accelerate the inference of the quantized model.

4.5. Ablation Study

In this section, we analyze the impact of different parameters on model performance and efficiency using StreamPETR-vov-1600x640 and OPEN-r101-1408x512 as two representative models.

Model	Backbone	ImageSize	Pruning	r	mAP \uparrow	NDS \uparrow	mATE \downarrow	mASE \downarrow	mAOE \downarrow	mAVE \downarrow	mAAE \downarrow	Inf. Time(ms) \downarrow	Decoder Time(ms) \downarrow
StreamPETR [33] (ICCV 2023)	ResNet50	704x256	-	-	38.01%	0.4822	0.6781	0.2763	0.6401	0.2831	0.2007	60.52	31.10
			ToMe	2000	36.12%	0.4651	0.7056	0.2806	0.6725	0.3011	0.1952	57.26(-5.39%)	29.38(-5.53%)
			Ours	2000	37.93%	0.4817	0.6787	0.2758	0.6390	0.2844	0.2016	51.68(-14.61%)	24.15(-22.35%)
	VovNet	1600x640	-	-	48.89%	0.5732	0.6096	0.2601	0.3882	0.2603	0.1944	288.07	64.93
			ToMe	12000	46.93%	0.5584	0.6301	0.2786	0.3876	0.2714	0.1951	277.60(-3.63%)	55.63(-14.32%)
			Ours	12000	48.85%	0.5738	0.6078	0.2603	0.3813	0.2613	0.1941	266.49(-7.47%)	46.16(-28.91%)
OPEN [14] (ECCV 2024)	ResNet50	704x256	-	-	47.02%	0.5657	0.5676	0.2702	0.4221	0.2321	0.2019	77.25	33.63
			ToMe	2000	45.10%	0.5495	0.5843	0.2719	0.4705	0.2373	0.1960	70.15(-9.19%)	29.48(-12.34%)
			Ours	2000	46.79%	0.5641	0.5691	0.2711	0.4232	0.2318	0.2029	63.31(-18.05%)	23.94(-28.81%)
	VovNet	800x320	-	-	52.07%	0.6128	0.5250	0.2566	0.2811	0.2148	0.1982	118.55	29.35
			ToMe	3000	49.21%	0.5926	0.5532	0.2594	0.3002	0.2248	0.1971	118.63(+0.07%)	29.70(+1.19%)
			Ours	3000	52.12%	0.6130	0.5250	0.2569	0.2810	0.2148	0.1985	110.21(-7.04%)	22.09(-24.74%)
	ResNet101	1408x512	-	-	51.80%	0.6043	0.5314	0.2679	0.3457	0.2095	0.1922	196.65	46.39
			ToMe	8000	50.36%	0.5939	0.5426	0.2676	0.3593	0.2160	0.1939	189.84(-3.46%)	40.42(-12.87%)
			Ours	8000	51.63%	0.6033	0.5336	0.2681	0.3439	0.2102	0.1927	184.69(-6.08%)	33.76(-27.23%)

Table 2. Compare to ToMe [1]. We set $n=2$ for both ToMe and tgGBC, $k = 175$ for tgGBC.

Model	Quantization	r	Inf. Time (ms) \downarrow	Time Reduce \uparrow
FocalPETR	-	-	1605.28	-
	-	12000	1406.66	-12.37%(1.14x)
	fp16	-	1600.71	-
	fp16	12000	1353.09	-15.47%(1.18x)
StreamPETR	-	-	3466.29	-
	-	21000	2946.40	-15.00%(1.18x)
	fp16	-	3446.85	-
	fp16	21000	2891.40	-16.11%(1.19x)

Table 3. Speed tested on OrangePi. We show the results of $n = 1, k = 175$. Reported FocalPETR(StreamPETR) uses ResNet18(VovNet) as backbone with an image resolution of 1408×512 (1600×640).

4.5.1. Influence of Parameters k , r and n

As illustrated in Fig. 4, there is no universally optimal value of k for all models. For some models, such as StreamPETR (Fig. 4 Top), the mAP exhibits an approximately linear correlation with k . However, for other models like OPEN (Fig. 4 Bottom), variations in k cause fluctuations in mAP within a certain range without a clear linear trend. After evaluating all experimental results, we determine that a reference value of $k = 175$ offers a reasonable balance between different models. k affects little to the inference time. The analysis can be found in Appendix B.

The parameter r represents the number of pruned keys. Intuitively, increasing r is expected to lead to performance degradation; however, the trend is not strictly monotonic in our experiments. For instance, for the StreamPETR, the mAP and the NDS at $r = 9000$ are equivalent to that at $r = 12000$ and even higher than that at $r = 4800$, as indicated by the points with triangles in Fig. 5. Overall, as r increases, model performance declines linearly. However, beyond a model-dependent threshold (about 80%-90% out of the N_k), the degradation rate accelerates significantly, as depicted in Fig. 5. For time reduction, there is an obvious trade-off between performance and inference time while r increases, as shown in Fig. 5 and Fig. 6.

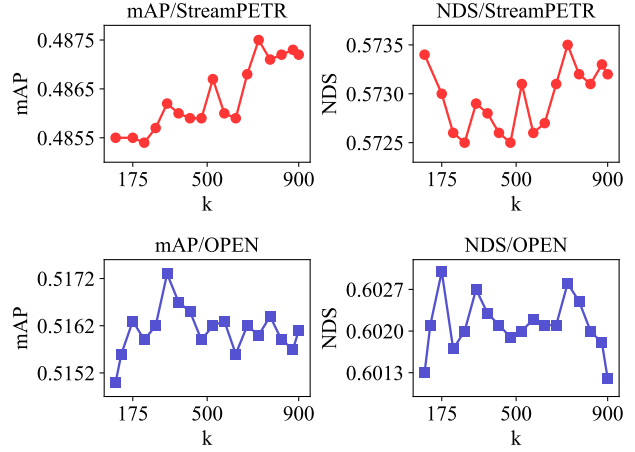


Figure 4. Ablation experiments for parameter k , with a range from 100 to 900. We use $r = 21000$ for StreamPETR, $r = 10000$ for OPEN and $n = 2$ for both models.

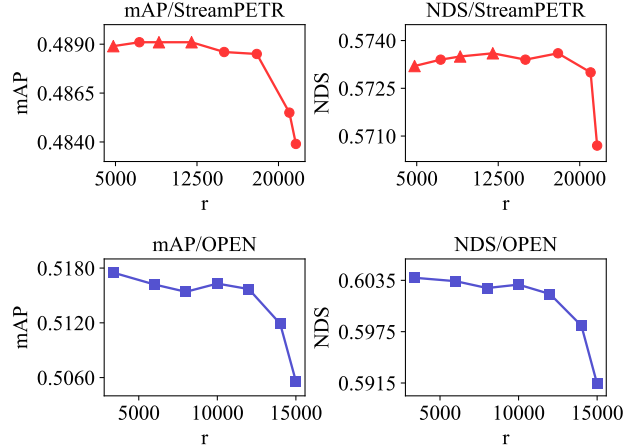


Figure 5. The mAP and NDS exhibit a negative correlation with the increase of r . When r exceeds a model-dependent threshold, the rate of performance degradation will accelerate sharply.

The parameter n represents the number of tgGBC layers inserted into the model. A smaller n (with a minimum value

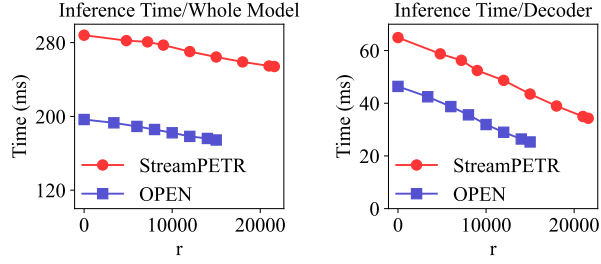


Figure 6. The inference time of the whole model and decoder time decrease linearly with the increase of r .

Model	n	mAP \uparrow	NDS \uparrow	Inf. Time(ms)	Decoder Time(ms)
StreamPETR	-	48.89%	0.5732	288.07	64.93
	5	48.92%	0.5744	267.40(-7.18%)	46.59(-28.25%)
	4	48.87%	0.5745	263.60(-8.49%)	44.25(-31.85%)
	3	48.21%	0.5702	259.08(-10.06%)	39.08(-39.81%)
	2	48.55%	0.5730	254.73(-11.57%)	34.98(-46.13%)
	1	47.84%	0.5695	251.24(-12.79%)	31.61(-51.32%)
	-	51.80%	0.6043	196.65	46.39
OPEN	5	51.73%	0.6037	190.07(-3.35%)	39.51(-14.83%)
	4	51.72%	0.6040	185.94(-5.45%)	36.29(-21.77%)
	3	51.61%	0.6021	183.77(-6.55%)	33.59(-27.59%)
	2	51.63%	0.6030	182.24(-7.33%)	31.92(-31.19%)
	1	51.65%	0.6027	179.55(-8.70%)	30.01(-35.31%)

Table 4. Ablation experiments for parameter n with $r = 21000$ (10000) and $k = 175$ for StreamPETR (OPEN).

of 1) means fewer tgGBC layers, requiring each layer to prune a larger number of keys. Intuitively, there is a trade-off between n , inference speed, and model performance: a lower n results in faster inference but can lead to greater performance degradation. As shown in Tab. 4, this argument is supported. However, similar to r , model performance does not decrease monotonically with increasing n . Instead, it fluctuates within a certain range, suggesting that the impact of n is model-dependent.

4.5.2. Impact of Classification Scores

Remove Classification Scores. To further evaluate the rationale behind the pruning criterion, we investigate the role of the classification score in the key selection process. Specifically, we examine whether incorporating classification scores is necessary for determining key importance. As shown in Eq. (10), we remove the classification score and instead compute key importance solely based on the column-wise sum of averaged attention weights:

$$S_j = \sum_{i=1}^{N_q} \left(\frac{1}{N_h} \sum_{i=1}^{N_q} A_{i,j}^h \right) \quad (10)$$

Since classification scores are excluded, we use $k = 900$ in tgGBC for comparison. As illustrated in Fig. 7, omitting the classification score leads to a significant drop in model performance as n decreases. This result highlights the importance of incorporating classification scores in maintaining the model’s stability.

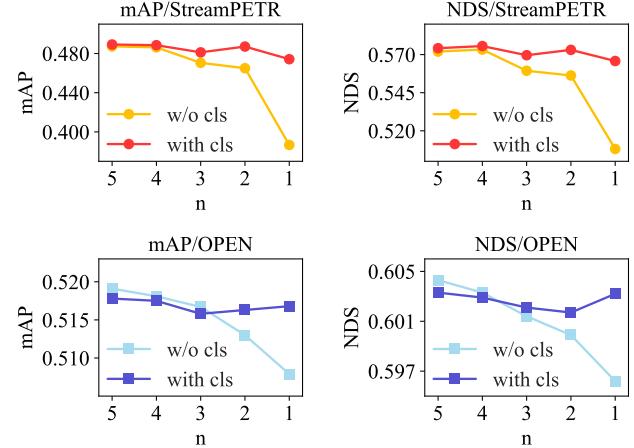


Figure 7. mAP and NDS for tgGBC with and w/o classification scores. We use $r=21000$ (10000) for StreamPETR(OPEN).

Model	Select	mAP \uparrow	NDS \uparrow	mATE \downarrow	mASE \downarrow	mAOE \downarrow	mAVE \downarrow	mAAE \downarrow
StreamPETR	-	48.89%	0.5732	0.6096	0.2601	0.3882	0.2603	0.1944
	max	48.55%	0.5730	0.6033	0.2626	0.3771	0.2611	0.1941
	mean	44.12%	0.5537	0.6452	0.2721	0.3799	0.2777	0.1944
	min	34.88%	0.4760	0.7199	0.2882	0.4694	0.3082	0.1977
OPEN	-	51.80%	0.6043	0.5314	0.2679	0.3457	0.2095	0.1922
	max	51.57%	0.6019	0.5368	0.2726	0.3493	0.2102	0.1905
	mean	49.57%	0.5839	0.5763	0.2795	0.3688	0.2210	0.1938
	min	47.65%	0.5703	0.6020	0.2837	0.3728	0.2299	0.1906

Table 5. Results of ablation experiments of the selection of classification scores, with a configuration of $n=2$, $k=175$ and $r=21000$ (12000) for StreamPETR(OPEN).

The Selection of Classification Scores. The first step of tgGBC involves selecting the maximum value from each classification vector, resulting in $\hat{C} \in \mathbb{R}^{N_q}$, as described in Eq. (6). To validate this point, we modify Eq. (6) by replacing the maximum selection with the average and minimum values of each classification vector. Results, presented in Tab. 5, confirm that selecting the maximum classification score yields superior performance, supporting the design choice in tgGBC.

For additional ablation studies and further exploration (Apply tgGBC to prune queries, evaluate it on fully converged models, integrate it into training, and extend it to 2D models), please refer to Appendix C.3 and Appendix D.

5. Conclusion

In this paper, we propose tgGBC, a runtime pruning method that removes redundant keys from transformer layers in 3D detectors. TgGBC requires no retraining or data calibration, making it a simple plug-and-play solution. Extensive experiments on multiple of state-of-the-art detectors demonstrate that our method effectively accelerates inference speed while preserving model performance, highlighting its practicality for real-world applications. We hope this work encourages further research into zero-shot pruning techniques for 3D object detection.

References

[1] Daniel Bolya, Cheng-Yang Fu, Xiaoliang Dai, Peizhao Zhang, Christoph Feichtenhofer, and Judy Hoffman. Token merging: Your vit but faster. In *International Conference on Learning Representations*, 2023. [1](#), [2](#), [7](#), [4](#)

[2] Holger Caesar, Varun Bankiti, Alex H. Lang, Sourabh Vora, Venice Erin Liang, Qiang Xu, Anush Krishnan, Yu Pan, Gi-an Carlo Baldan, and Oscar Beijbom. nuscenes: A multi-modal dataset for autonomous driving. In *Proceedings of the IEEE/CVF Conference on Computer Vision and Pattern Recognition (CVPR)*, 2020. [4](#)

[3] Nicolas Carion, Francisco Massa, Gabriel Synnaeve, Nicolas Usunier, Alexander Kirillov, and Sergey Zagoruyko. End-to-end object detection with transformers. In *European Conference on Computer Vision*, pages 213–229. Springer, 2020. [2](#)

[4] Jiahao Chang, Shuo Wang, Hai-Ming Xu, Zehui Chen, Chenhongyi Yang, and Feng Zhao. Detrdistill: A universal knowledge distillation framework for detr-families. In *Proceedings of the IEEE/CVF International Conference on Computer Vision*, pages 6898–6908, 2023. [1](#)

[5] Siran Chen, Yue Ma, Yu Qiao, and Yali Wang. M-bev: Masked bev perception for robust autonomous driving. In *Proceedings of the AAAI Conference on Artificial Intelligence*, 2024. [1](#), [2](#), [5](#)

[6] Tianlong Chen, Yu Cheng, Zhe Gan, Lu Yuan, Lei Zhang, and Zhangyang Wang. Chasing sparsity in vision transformers: An end-to-end exploration. *Advances in Neural Information Processing Systems*, 34:19974–19988, 2021. [1](#)

[7] Alexey Dosovitskiy. An image is worth 16x16 words: Transformers for image recognition at scale. *arXiv preprint arXiv:2010.11929*, 2020. [1](#), [3](#)

[8] Angela Fan, Edouard Grave, and Armand Joulin. Reducing transformer depth on demand with structured dropout. *arXiv preprint arXiv:1909.11556*, 2019. [1](#)

[9] Yuxin Fang, Quan Sun, Xinggang Wang, Tiejun Huang, Xinlong Wang, and Yue Cao. Eva-02: A visual representation for neon genesis. *Image and Vision Computing*, 149:105171, 2024. [1](#), [3](#)

[10] Mohsen Fayyaz, Soroush Abbasi Koohpayegani, Farnoush Rezaei Jafari, Sunando Sengupta, Hamid Reza Vaezi Jozé, Eric Sommerladé, Hamed Pirsiaavash, and Jürgen Gall. Adaptive token sampling for efficient vision transformers. In *European Conference on Computer Vision*, pages 396–414. Springer, 2022. [1](#), [2](#)

[11] Jonathan Frankle and Michael Carbin. The lottery ticket hypothesis: Finding sparse, trainable neural networks. *arXiv preprint arXiv:1803.03635*, 2018. [1](#)

[12] Kaiming He, Xiangyu Zhang, Shaoqing Ren, and Jian Sun. Deep residual learning for image recognition. In *Proceedings of the IEEE conference on computer vision and pattern recognition*, pages 770–778, 2016. [1](#)

[13] Geoffrey Hinton, Oriol Vinyals, and Jeff Dean. Distilling the knowledge in a neural network. *arXiv preprint arXiv:1503.02531*, 2015. [1](#)

[14] Jinghua Hou, Tong Wang, Xiaoqing Ye, Zhe Liu, Xiao Tan, Errui Ding, Jingdong Wang, and Xiang Bai. Open: Object-wise position embedding for multi-view 3d object detection. In *European Conference on Computer Vision*, 2024. [1](#), [2](#), [5](#), [7](#)

[15] Xiaohui Jiang, Shuailin Li, Yingfei Liu, Shihao Wang, Fan Jia, Tiancai Wang, Lijin Han, and Xiangyu Zhang. Far3d: Expanding the horizon for surround-view 3d object detection. In *Proceedings of the AAAI Conference on Artificial Intelligence*, pages 2561–2569, 2024. [1](#), [4](#)

[16] Samir Khaki and Konstantinos N Plataniotis. The need for speed: Pruning transformers with one recipe. In *The Twelfth International Conference on Learning Representations*, 2024. [1](#), [2](#)

[17] Woosuk Kwon, Sehoon Kim, Michael W Mahoney, Joseph Hassoun, Kurt Keutzer, and Amir Gholami. A fast post-training pruning framework for transformers. *Advances in Neural Information Processing Systems*, 35:24101–24116, 2022. [1](#), [2](#)

[18] Youngwan Lee and Jongyoul Park. Centermask: Real-time anchor-free instance segmentation. In *Proceedings of the IEEE/CVF conference on computer vision and pattern recognition*, pages 13906–13915, 2020. [1](#)

[19] Yinhao Li, Zheng Ge, Guanyi Yu, Jinrong Yang, Zengran Wang, Yukang Shi, Jianjian Sun, and Zeming Li. Bevdepth: Acquisition of reliable depth for multi-view 3d object detection. In *Proceedings of the AAAI Conference on Artificial Intelligence*, pages 1477–1485, 2023. [1](#)

[20] Zhiqi Li, Wenhui Wang, Hongyang Li, Enze Xie, Chong-hao Sima, Tong Lu, Yu Qiao, and Jifeng Dai. Bevformer: Learning bird’s-eye-view representation from multi-camera images via spatiotemporal transformers. In *European Conference on Computer Vision*, pages 1–18. Springer, 2022. [1](#)

[21] Chen Liang, Simiao Zuo, Qingru Zhang, Pengcheng He, Weizhu Chen, and Tuo Zhao. Less is more: Task-aware layer-wise distillation for language model compression. In *International Conference on Machine Learning*, pages 20852–20867. PMLR, 2023. [1](#)

[22] Feng Liu, Tengteng Huang, Qianjing Zhang, Haotian Yao, Chi Zhang, Fang Wan, Qixiang Ye, and Yanzhao Zhou. Ray denoising: Depth-aware hard negative sampling for multi-view 3d object detection. In *European Conference on Computer Vision*. Springer, 2024. [1](#), [4](#)

[23] Haisong Liu, Yao Teng, Tao Lu, Haiguang Wang, and Limin Wang. Sparsebev: High-performance sparse 3d object detection from multi-camera videos. In *Proceedings of the IEEE/CVF International Conference on Computer Vision*, pages 18580–18590, 2023. [1](#), [4](#)

[24] Yingfei Liu, Tiancai Wang, Xiangyu Zhang, and Jian Sun. Petr: Position embedding transformation for multi-view 3d object detection. In *European Conference on Computer Vision*, pages 531–548. Springer, 2022. [1](#), [2](#), [5](#)

[25] Yingfei Liu, Junjie Yan, Fan Jia, Shuailin Li, Aqi Gao, Tiancai Wang, and Xiangyu Zhang. PetrV2: A unified framework for 3d perception from multi-camera images. In *Proceedings of the IEEE/CVF International Conference on Computer Vision (ICCV)*, pages 3262–3272, 2023. [1](#)

[26] Yifei Liu, Mathias Gehrig, Nico Messikommer, Marco Caninici, and Davide Scaramuzza. Revisiting token pruning for

object detection and instance segmentation. In *Proceedings of the IEEE/CVF Winter Conference on Applications of Computer Vision*, pages 2658–2668, 2024. 1

[27] Paul Michel, Omer Levy, and Graham Neubig. Are sixteen heads really better than one? *Advances in neural information processing systems*, 32, 2019. 1

[28] Changyong Shu, Jiajun Deng, Fisher Yu, and Yifan Liu. 3dppe: 3d point positional encoding for multi-camera 3d object detection transformers. In *Proceedings of the IEEE/CVF International Conference on Computer Vision*, 2023. 1, 2, 5

[29] Hugo Touvron, Matthieu Cord, Matthijs Douze, Francisco Massa, Alexandre Sablayrolles, and Herve Jegou. Training data-efficient image transformers & distillation through attention. In *International Conference on Machine Learning*, pages 10347–10357, 2021. 3

[30] Ashish Vaswani, Noam Shazeer, Niki Parmar, Jakob Uszkoreit, Llion Jones, Aidan N Gomez, Łukasz Kaiser, and Illia Polosukhin. Attention is all you need. *Advances in neural information processing systems*, 30, 2017. 2

[31] Hongjie Wang, Bhishma Dedhia, and Niraj K Jha. Zeroprune: Zero-shot token pruning through leveraging of the attention graph in pre-trained transformers. In *Proceedings of the IEEE/CVF Conference on Computer Vision and Pattern Recognition*, pages 16070–16079, 2024. 1, 2

[32] Shihao Wang, Xiaohui Jiang, and Ying Li. Focal-petr: Embracing foreground for efficient multi-camera 3d object detection. *IEEE Transactions on Intelligent Vehicles*, 2023. 1, 2, 5

[33] Shihao Wang, Yingfei Liu, Tiancai Wang, Ying Li, and Xiangyu Zhang. Exploring object-centric temporal modeling for efficient multi-view 3d object detection. In *Proceedings of the IEEE/CVF International Conference on Computer Vision*, pages 3621–3631, 2023. 1, 2, 5, 7

[34] Yue Wang, Vitor Campagnolo Guizilini, Tianyuan Zhang, Yilun Wang, Hang Zhao, and Justin Solomon. Detr3d: 3d object detection from multi-view images via 3d-to-2d queries. In *Conference on Robot Learning*, pages 180–191. PMLR, 2022. 1, 4

[35] Zitian Wang, Zehao Huang, Jiahui Fu, Naiyan Wang, and Si Liu. Object as query: Lifting any 2d object detector to 3d detection. In *Proceedings of the IEEE/CVF International Conference on Computer Vision*, pages 3791–3800, 2023. 1, 5

[36] Lizhen Xu, Shanmin Pang, Wenzhao Qiu, Zehao Wu, Xiu Bai, Kuizhi Mei, and Jianru Xue. Redundant queries in detr-based 3d detection methods: Unnecessary and prunable, 2024. 4

[37] Chenyu Yang, Yuntao Chen, Hao Tian, Chenxin Tao, Xizhou Zhu, Zhaoxiang Zhang, Gao Huang, Hongyang Li, Yu Qiao, Lewei Lu, Jie Zhou, and Jifeng Dai. Bevformer v2: Adapting modern image backbones to bird’s-eye-view recognition via perspective supervision. In *2023 IEEE/CVF Conference on Computer Vision and Pattern Recognition (CVPR)*, pages 17830–17839, 2023. 1

[38] Fang Yu, Kun Huang, Meng Wang, Yuan Cheng, Wei Chu, and Li Cui. Width & depth pruning for vision transformers. In *Proceedings of the AAAI Conference on Artificial Intelligence*, pages 3143–3151, 2022. 1

[39] Lu Yu and Wei Xiang. X-pruner: explainable pruning for vision transformers. In *Proceedings of the IEEE/CVF conference on computer vision and pattern recognition*, pages 24355–24363, 2023. 1

[40] Dingyuan Zhang, Dingkang Liang, Zichang Tan, Xiaoqing Ye, Cheng Zhang, Jingdong Wang, and Xiang Bai. Make your vit-based multi-view 3d detectors faster via token compression. In *European Conference on Computer Vision*, 2024. 1, 2, 5

[41] Xizhou Zhu, Weijie Su, Lewei Lu, Bin Li, Xiaogang Wang, and Jifeng Dai. Deformable detr: Deformable transformers for end-to-end object detection. In *International Conference on Learning Representations*, 2021. 1, 4

Accelerate 3D Object Detection Models via Zero-Shot Attention Key Pruning

Supplementary Material

A. Query-based 3D Detectors

A.1. Overall Architecture

DETR-based methods have become the mainstream approach for 3D object detection. As shown in Fig. 8 (a), these methods typically take multi-view images as input and use an image backbone to extract image features F . Subsequently, F is fed into a transformer decoder along with pre-defined queries Q for interaction. Represented by PETR, **dense methods** adopt global attention, allowing Q to interact with F globally. In contrast, **sparse methods** such as DETR3D and Far3D employ deformable attention, selecting only a subset of F for interaction with Q . The output of the Transformer Decoder maintains the same shape as the predefined queries Q . It is passed to classification branches and regression branches to obtain classification scores and bounding boxes B . The bounding boxes B not only contain object location information but also include object size, orientation, velocity, and additional attributes (e.g., whether a pedestrian is standing, walking, or sitting). During training, DETR-based methods use a bipartite matching strategy to associate predictions with ground truth and compute classification and localization losses. Since ground truth is unavailable during inference, the model selects the final predictions based on classification scores.

The Transformer decoder used in 3D detectors has a structure of self-attention followed by cross-attention. The self-attention module of the first layer takes pre-defined query Q as input, and its output, together with image features, will be fed into the following cross-attention module. The output of the cross-attention module will be taken as input by the next layer's self-attention module. Our method uses the attention map generated by the cross-attention modules.

A.2. Advantages of Dense Methods over Sparse Methods

Since the introduction of DETR, DETR-based methods have gradually gained prominence in various vision tasks, including image classification, 2D object detection, 3D object detection, semantic segmentation, and object tracking. However, DETR-based methods also have several drawbacks, such as high computational cost and slow inference speed. One major issue is their slow convergence rate. DETR requires training for several hundred epochs on the COCO dataset before convergence. To address this, DeformableDETR was proposed. By utilizing reference points for local feature sampling, DeformableDETR significantly speeds up convergence, requiring only 50 epochs on the

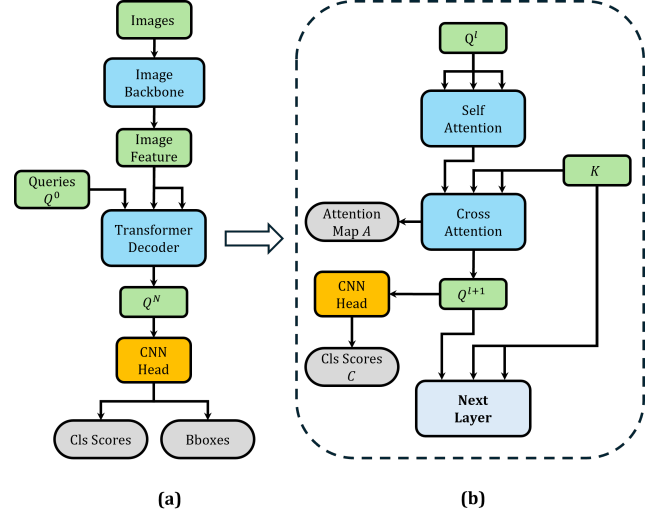


Figure 8. (a) Overall architecture of query-based 3D detectors. All dense models share the same overall structure: an image backbone followed by a transformer decoder. The transformer decoder consists of multiple stacked transformer layers. (b) The transformer layer used in the transformer decoder in (a). Each layer has a self-attention module and a cross-attention module. A CNN head can be used following the cross-attention module, which inputs updated queries and outputs the classification scores. We use attention map $A \in \mathbb{R}^{N_q \times N_k}$ and classification scores $C \in \mathbb{R}^{N_q}$ to calculate each key's importance score.

COCO dataset to achieve the same performance as DETR trained for 500 epochs. In the 3D object detection domain, sparse methods have been introduced to accelerate model convergence while also reducing the computational burden of the decoder to some extent.

However, our comparison reveals that the overall model does not achieve a significant increase in inference speed, nor does it reduce memory consumption. In some cases, sacrificing performance necessitates additional compensatory mechanisms, introducing extra parameters that increase memory usage.

We selected state-of-the-art dense and sparse methods, OPEN and SparseBEV, respectively, for comparison. From the comparison in Tab. 6, it can be observed that when using the same backbone and image resolution, SparseBEV performs worse than OPEN on the nuScenes validation set. In terms of memory usage, during inference, SparseBEV consumes more memory than OPEN when using the same backbone and image resolution. Regarding inference speed, SparseBEV does not show a significant advantage over OPEN.

Model	Backbone	ImageSize	mAP \uparrow	NDS \uparrow	mATE \downarrow	mASE \downarrow	mAOE \downarrow	mAVE \downarrow	mAAE \downarrow	Mem. (MiB) \downarrow	Inf. Time (ms) \downarrow
SparseBEV	ResNet50	704x256	45.45%	0.5559	0.5984	0.2706	0.4124	0.2435	0.1865	5640	77.72
	ResNet101	1408x512	50.12%	0.5920	0.5621	0.2648	0.3211	0.2427	0.1947	15386	193.25
OPEN	ResNet50	704x256	47.02%	0.5657	0.5676	0.2702	0.4221	0.2321	0.2019	4062	77.25
	ResNet101	1408x512	51.80%	0.6043	0.5314	0.2679	0.3457	0.2095	0.1922	10696	196.55

Table 6. Comparison of SparseBEV and OPEN.

In summary, while current dense methods converge more slowly than sparse methods, they offer advantages in performance and memory usage, without showing a clear disadvantage in inference speed. Due to their strong overall advantages, new dense methods continue to emerge. This further highlights the importance of our work.

B. Analysis of Computation Cost of Importance Scores

The FLOPs of Matrix Multiplication. Assume there are two matrices $A \in \mathbb{R}^{N \times C}$, $B \in \mathbb{R}^{M \times C}$. When computing $AB^T \in \mathbb{R}^{N \times M}$, each row $A_i \in \mathbb{R}^C$ of A is multiplied by each column $B_j \in \mathbb{R}^C$ of B^T , which requires C multiplications and $C - 1$ additions. Since A has N rows and B^T has M columns, the total computational complexity is:

$$\begin{aligned} F_{\text{mat_mul}} &= N \times M \times (C + (C - 1)) \\ &= N \times M \times (2C - 1) \end{aligned} \quad (11)$$

The FLOPs of a Multi-head Attention. Given the input $Q \in \mathbb{R}^{N_q \times E}$, $K \in \mathbb{R}^{N_k \times E}$, and $V \in \mathbb{R}^{N_k \times E}$, a multi-head attention module with H heads includes the operations shown in Eq. (1)-Eq. (4).

In Eq. (1), the operations involve matrix multiplications: one between $Q \in \mathbb{R}^{N_q \times E}$ and $\mathbb{R}^{E \times E}$, and two between $K, V \in \mathbb{R}^{N_k \times E}$ and $\mathbb{R}^{E \times E}$, with a total FLOPs:

$$N_k \cdot (4E^2 - 2E) + 2N_q E^2 - N_q E \quad (12)$$

In Eq. (3), where $q^h \in \mathbb{R}^{N_q \times E_h}$, $k^h \in \mathbb{R}^{N_k \times E_h}$:

1) It first calculates a matrix multiplication $q^h \times (k^h)^T$ with FLOPs $N_q N_k (2E_h - 1)$. For total H heads, FLOPs are:

$$N_k \cdot (2N_q E - N_q H) \quad (13)$$

2) Next, a square root is performed to get \sqrt{E} with FLOPs 1.

3) Each element of $(q^h \times (k^h)^T)$ divides \sqrt{E} , resulting in FLOPs of $N_q N_k$. For total H heads, FLOPs are:

$$N_k \cdot N_q H \quad (14)$$

4) For the Softmax operation with a vector of shape \mathbb{R}^N as input, it performs N exponentiations, $N - 1$ additions and N divisions. Hence, Softmax (\cdot) in Eq. (3) has $N_q (3N_k - 1)$ FLOPs. For total H heads, FLOPs are:

$$N_k \cdot 3N_q H - N_q H \quad (15)$$

5) Next, $O^h = A^h \times v^h$ has $N_q E_h (2N_k - 1)$ FLOPs. For total H heads, FLOPs are:

$$N_k \cdot 2N_q E - N_q E \quad (16)$$

Hence, Eq. (3) and $O^h = A^h \times v^h$ has FLOPs:

$$N_k \cdot (4N_q E + 3N_q H) - N_q H - N_q E + 1 \quad (17)$$

Finally, Eq. (4) has FLOPs:

$$2N_q E^2 - N_q E \quad (18)$$

In summary, according to Eq. (12), Eq. (17) and Eq. (18), a single multi-head attention module with H heads contains FLOPs as follows:

$$\begin{aligned} F_{\text{mha}}(N_k) &= \lambda N_k + b \\ \lambda &= 4E^2 - 2E + 4N_q E + 3N_q H \\ b &= 4N_q E^2 - 3N_q E - N_q H + 1 \end{aligned} \quad (19)$$

A transformer layer contains a self-attention module, a cross-attention module, two layer normalizations and a feed-forward network. Among these, only cross-module is related to *key* with $Q \in \mathbb{R}^{N_q \times E}$, $K, V \in \mathbb{R}^{N_k \times E}$ as inputs. Hence, its FLOPs are:

$$F_{\text{CA}}(N_k) = F_{\text{mha}}(N_k) \quad (20)$$

Cost of Computing Importance Scores. To calculate importance scores, we first need to calculate averaged attention maps A , which involves $N_q N_k (H - 1)$ additions and $N_q N_k$ divisions, with total FLOPs $N_q N_k H$. Next, we calculate $S_0 = A \odot \tilde{C}$, which contains $N_q \times N_k$ multiplications. After selection, we compute the sum along the column of S_1 (Eq. (9)), which needs $N_k (k - 1)$ additions. In total, the FLOPs of calculating importance scores are:

$$F_S = N_q N_k H + N_q N_k + N_k (k - 1) \quad (21)$$

Considering a transformer module with L layers applying tgGBC with r, n, k .

The FLOPs before pruning:

$$F_{\text{before}} = L \cdot F_{\text{CA}}(N_k) \quad (22)$$

Model	Backbone	ImageSize	N_k	r	GFLOPs	Reduced FLOPs
StreamPETR	VovNet	1600x640	24000	-	174.91	-
OPEN	ResNet101	1408x512	16896	21000	123.55	-64.88%
				12000	58.84	-52.37%

Table 7. FLOPs reduced of the transformer module after pruning. We show the results of StreamPETR and OPEN with $n = 2, k = 175$ for both models. $1 \text{ GFLOPs} = 10^9 \text{ FLOPs}$.

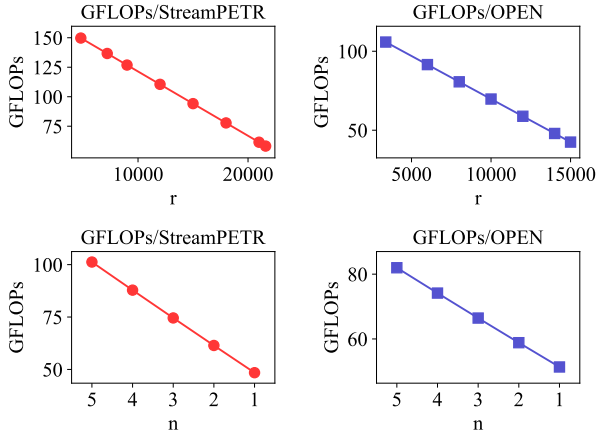


Figure 9. FLOPs decrease with the increase r and the decrease n . StreamPETR (OPEN) shown in the figure uses VovNet (ResNet101) and an image size of 1600×640 (1408×512). For the first line, both models use $n=2$ and $k = 175$. For the second line, StreamPETR (OPEN) uses $k = 175$ and $r=21000$ (12000).

The FLOPs after pruning:

$$\begin{aligned} F_{\text{after}} = & \sum_{i=0}^n F_{\text{CA}} \left(N_k - i \cdot \frac{r}{n} \right) \\ & + \max(0, L - (n + 1)) \cdot F_{\text{CA}}(N_k - r) \quad (23) \\ & + \sum_{i=0}^{n-1} F_{\text{S}} \left(N_k - i \cdot \frac{r}{n} \right) \end{aligned}$$

For different models, we calculate FLOPs before and after pruning as exhibited in Tab. 7.

According to Eq. (23), the FLOPs decrease linearly with the increase of r and the decrease of n , as shown in Fig. 9.

As described in Sec. 4.5, the impact of k on inference time is negligible. This is because when k varies within the range $[1, N_q]$, its effect on FLOPs is minimal, as shown in Fig. 10. No matter how k changes, the computational cost of the Cross-Attention module varies by no more than 0.1 GFLOPs. Compared to the effects of r and n , the influence of k on inference time can be ignored.

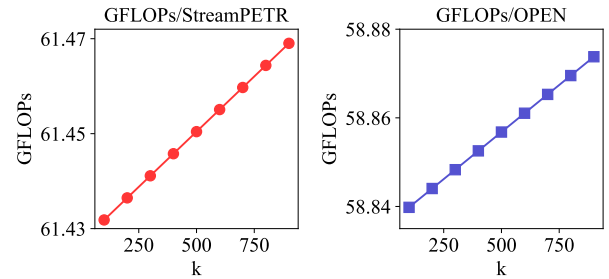


Figure 10. When k changes, there is almost no change in FLOPs.

C. More Results

C.1. Optimal Results

As described in Sec. 4.2, to facilitate clearer comparison and save space, we uniformly report the results with $n = 2$ and $k = 175$. However, this is not the optimal configuration for every model. Here, the optimal configuration refers to the maximum value of r and the minimum value of n that can be applied when the mAP and NDS decrease by no more than 1%. For the vast majority of models, we can directly use $n = 1$ for pruning, as shown in Tab. 8. For models that have already achieved optimal results, as shown in Tab. 1 (e.g., PETR-vov, FocalPETR, MV2D, StreamPETR-vov), we do not repeat the results here.

C.2. More Comparison to ToMe

As described in Sec. 4.3, our method is the first to apply zero-shot pruning to 3D object detection models. Therefore, there are no similar methods available for a fair comparison. However, we can attempt to transfer zero-shot pruning methods from the Vision Transformer (ViT) domain to 3D object detection models. Among these methods, ATS relies on a classification token specifically designed for classification tasks, and Zero-TPrune depends on a square-shaped attention map. Neither of these features exists in 3D object detection methods, making it impossible to transfer ATS and Zero-TPrune to 3D object detection. In contrast, ToMe does not have a strong dependency on the shape of the attention map or the classification token. Therefore, we selected ToMe as the comparison method.

As shown in the Tab. 9, for PETR and MV2D, ToMe performs extremely poorly—when pruning only 50% of the keys, the model’s performance completely collapses, with mAP dropping by more than 10%. In contrast, tgGBC can maintain model performance. Even when $n = 1$ and some results are suboptimal, with mAP dropping by more than 1%, the model does not degrade into an unusable state.

Model	Backbone	ImageSize	N_k	r	n	k	mAP ↑	NDS ↑	mATE ↓	mASE ↓	mAOE ↓	mAVE ↓	mAAE ↓	Inf. Time(ms) ↓
PETR	ResNet50	1408x512	16896	-	-	-	31.74%	0.3669	0.8392	0.2797	0.6145	0.9521	0.2322	131.94
			10000	1	175		30.78%	0.3579	0.8540	0.2832	0.6168	0.9703	0.2354	110.35(-16.36%)
PETRv2	VovNet	800x320	12000	-	-	-	41.05%	0.5024	0.7232	0.2692	0.4529	0.3896	0.1932	157.52
			8000	2	175		40.29%	0.4918	0.7333	0.2750	0.4526	0.4428	0.1930	139.33(-11.55%)
StreamPETR	ResNet50	704x256	4224	-	-	-	38.01%	0.4822	0.6781	0.2763	0.6401	0.2831	0.2007	60.52
			2000	1	900		37.96%	0.4822	0.6828	0.2757	0.6373	0.2794	0.2009	51.59(-14.76%)
3DPPE	VovNet	800x320	6000	-	-	-	39.81%	0.4460	0.7040	0.2699	0.4951	0.8438	0.2177	125.13
			3000	1	175		39.57%	0.4430	0.7089	0.2729	0.4974	0.8496	0.2201	94.09(-24.81%)
M-BEV	VovNet	800x320	12000	-	-	-	35.14%	0.4640	0.7300	0.2717	0.4980	0.4324	0.1845	178.87
			6000	1	175		34.91%	0.4600	0.7379	0.2727	0.5049	0.4428	0.1873	150.93(-15.63%)
	ResNet50	704x256	4224	-	-	-	47.02%	0.5657	0.5676	0.2702	0.4221	0.2321	0.2019	77.25
			2000	1	900		46.88%	0.5636	0.5687	0.2721	0.2332	0.2315	0.2026	63.31(-18.05%)
OPEN	VovNet	800x320	6000	-	-	-	52.07%	0.6128	0.5250	0.2566	0.2811	0.2148	0.1982	118.55
			3000	1	175		52.12%	0.6130	0.5250	0.2569	0.2810	0.2148	0.1985	110.21(-7.04%)
	ResNet101	1408x512	16896	-	-	-	51.80%	0.6043	0.5314	0.2679	0.3457	0.2095	0.1922	196.55
			12000	1	175		51.47%	0.6018	0.5356	0.2691	0.3446	0.2131	0.1931	174.70(-11.16%)
ToC3D	ToC3DViT	1600x800	30000	-	-	-	54.20%	0.6187	0.5589	0.2571	0.2716	0.2353	0.2007	863.47
			27000	1	900		53.31%	0.6121	0.5736	0.2591	0.2713	0.2381	0.2029	809.48(-6.25%)

Table 8. Optimal results for each model.

Model	Backbone	ImageSize	Pruning	r	n	mAP ↑	NDS ↑	mATE ↓	mASE ↓	mAOE ↓	mAVE ↓	mAAE ↓
PETR	ResNet50	1408x512	ToMe	-	-	31.74%	0.3669	0.8392	0.2797	0.6145	0.9521	0.2322
				8000	2	30.48%	0.3543	0.8708	0.2816	0.6091	0.9852	0.2342
				8000	1	29.81%	0.3490	0.8714	0.2823	0.6173	0.9878	0.2418
				12000	2	29.63%	0.3461	0.8859	0.2836	0.6198	0.9895	0.2412
			Ours	8000	2	31.22%	0.3639	0.8436	0.2808	0.6133	0.9517	0.2329
				8000	1	31.58%	0.3651	0.8418	0.2801	0.6148	0.9576	0.2330
				12000	2	30.78%	0.3579	0.8540	0.2832	0.6168	0.9703	0.2354
	VovNet	1600x640	ToMe	-	-	40.45%	0.4517	0.7287	0.2706	0.4485	0.8399	0.2178
				12000	2	21.88%	0.2835	0.9517	0.4471	0.5913	1.0230	0.2688
				12000	1	27.17%	0.3350	0.8710	0.3560	0.5512	0.9959	0.2342
				18000	2	26.58%	0.3162	0.9143	0.4300	0.5663	1.0210	0.2564
	3DPPE	VovNet	Ours	12000	2	40.42%	0.4502	0.7305	0.2702	0.4501	0.8512	0.2172
				12000	1	39.37%	0.4425	0.7429	0.2722	0.4592	0.8517	0.2174
				18000	2	39.53%	0.4432	0.7482	0.2720	0.4538	0.8539	0.2167
			ToMe	-	-	39.81%	0.4460	0.7040	0.2699	0.4951	0.8438	0.2177
				2000	2	39.56%	0.4432	0.7083	0.2715	0.4972	0.8490	0.2198
				1		36.99%	0.4197	0.7500	0.2719	0.5337	0.8735	0.2233
			Ours	2000	2	39.74%	0.4449	0.7057	0.2707	0.4956	0.8465	0.2202
				1		39.57%	0.4430	0.7089	0.2729	0.4974	0.8496	0.2201
				2000	1							
	MV2D	ResNet50	ToMe	-	-	44.92%	0.5399	0.6246	0.2657	0.3840	0.4009	0.1722
				50%	2	13.62%	0.2754	0.9028	0.3472	0.7737	0.6777	0.2261
				1		13.45%	0.2721	0.9000	0.3477	0.7890	0.6864	0.2286
			Ours	50%	2	44.11%	0.5384	0.6248	0.2657	0.3844	0.4024	0.1717
				1		41.17%	0.5183	0.6289	0.2693	0.3887	0.4165	0.1717

Table 9. More results of comparison to ToMe [1]. Due to the use of bipartite matching, ToMe cannot prune more than 50% of keys in one layer; hence, some results of $r > N_k/2$ are lacking.

C.3. More Ablation Experiments

We report additional results for different values of r, n, k in Tab. 10. As discussed in the main text Sec. 4.2, the optimal parameter selection varies across different models. If we

set a 1% mAP drop as the threshold, the maximum number of keys that can be pruned varies depending on the model, and the same applies to n . When r is too large or $n = 1$, some models may experience a performance drop exceeding 1%. However, the model performance does not com-

Model	Backbone	ImageSize	<i>r</i>	<i>n</i>	<i>k</i>	mAP \uparrow	NDS \uparrow	mATE \downarrow	mASE \downarrow	mAOE \downarrow	mAVE \downarrow	mAAE \downarrow	
ResNet50	704x256	2000	-	-	-	38.01%	0.4822	0.6781	0.2763	0.6401	0.2831	0.2007	
			5	150	38.04%	0.4824	0.6787	0.2760	0.6388	0.2838	0.2007		
			4	175	38.04%	0.4826	0.6795	0.2761	0.6367	0.2826	0.2014		
			3	150	37.91%	0.4813	0.6819	0.2761	0.6385	0.2832	0.2025		
			2	175	37.91%	0.4817	0.6787	0.2758	0.6390	0.2844	0.2016		
	12000	12000	1	900	37.96%	0.4822	0.6828	0.2757	0.6373	0.2794	0.2009		
			-	-	-	48.89%	0.5732	0.6096	0.2601	0.3882	0.2603	0.1944	
			5	900	48.92%	0.5734	0.6089	0.2603	0.3884	0.2601	0.1942		
			4	900	48.90%	0.5735	0.6082	0.2601	0.3871	0.2598	0.1946		
			3	900	48.89%	0.5736	0.6076	0.2599	0.3870	0.2595	0.1940		
StreamPETR	VovNet	1600x640	2	900	48.95%	0.5741	0.6074	0.2605	0.3858	0.2594	0.1937		
			1	175	48.85%	0.5738	0.6078	0.2603	0.3813	0.2613	0.1941		
			5	900	48.95%	0.5743	0.6059	0.2605	0.3833	0.2602	0.1944		
			4	900	48.94%	0.5744	0.6064	0.2604	0.3821	0.2600	0.1943		
			18000	3	900	48.67%	0.5738	0.6054	0.2617	0.3701	0.2627	0.1955	
	21000	21000	2	900	48.85%	0.5738	0.6054	0.2617	0.3701	0.2627	0.1955		
			1	900	48.62%	0.5734	0.6087	0.2613	0.3705	0.2628	0.1942		
			5	900	48.92%	0.5742	0.6063	0.2604	0.3820	0.2611	0.1942		
			4	900	48.85%	0.5756	0.6015	0.2614	0.3659	0.2616	0.1966		
			3	175	48.21%	0.5702	0.6089	0.2619	0.3751	0.2669	0.1957		
OPEN	VovNet	800x320	2	900	48.71%	0.5731	0.6052	0.2622	0.3822	0.2618	0.1933		
			1	900	47.87%	0.5695	0.6071	0.2635	0.3625	0.2692	0.1952		
			-	-	-	47.02%	0.5657	0.5676	0.2702	0.4221	0.2321	0.2019	
			5	900	46.98%	0.5648	0.5669	0.2706	0.4303	0.2319	0.2015		
			4	900	47.03%	0.5649	0.5680	0.2705	0.4296	0.2321	0.2017		
	3000	2000	3	900	47.02%	0.5642	0.5685	0.2706	0.4345	0.2324	0.2028		
			2	175	46.85%	0.5637	0.5682	0.2705	0.4311	0.2325	0.2031		
			1	900	46.88%	0.5636	0.5687	0.2721	0.4332	0.2315	0.2026		
			-	-	-	52.07%	0.6128	0.5250	0.2566	0.2811	0.2148	0.1982	
			5	175	52.07%	0.6126	0.5261	0.2566	0.2818	0.2147	0.1985		
ResNet101	1408x512	10000	4	175	52.06%	0.6124	0.5267	0.2566	0.2823	0.2144	0.1987		
			3	175	52.08%	0.6127	0.5254	0.2565	0.2814	0.2149	0.1986		
			2	175	52.09%	0.6129	0.5249	0.2569	0.2808	0.2146	0.1986		
			1	175	52.12%	0.6130	0.5250	0.2569	0.2810	0.2148	0.1985		
			-	-	-	51.80%	0.6043	0.5314	0.2679	0.3457	0.2095	0.1922	
	12000	12000	5	900	51.78%	0.6033	0.5339	0.2694	0.3509	0.2101	0.1916		
			4	900	51.75%	0.6029	0.5333	0.2693	0.3544	0.2109	0.1907		
			3	900	51.58%	0.6021	0.5372	0.2695	0.3496	0.2107	0.1914		
			2	900	51.63%	0.6017	0.5386	0.2713	0.3542	0.2102	0.1906		
			1	900	51.68%	0.6032	0.5357	0.2691	0.3443	0.2110	0.1921		

Table 10. More results with different r , n and k for StreamPETR and OPEN.

pletely degrade into an unusable state but remains at a functional level.

We have conducted extensive experiments for each model, but due to space limitations, only a portion of the results can be presented here. Please refer to our GitHub repository for additional experimental results.

D. Further Exploration

D.1. Why Some Models Improve in Performance

We can observe that for some models, the mAP and NDS increase rather than decrease after pruning, such as FocalPETR-vov-800x320 in Tab. 1 and StreamPETR-r50-

Model	r	q	mAP \uparrow	NDS \uparrow	mATE \downarrow	mASE \downarrow	mAOE \downarrow	mAVE \downarrow	mAAE \downarrow	Dec. Time (ms)
StreamPETR	-	-	48.89%	0.5732	0.6096	0.2601	0.3882	0.2603	0.1944	64.93
	21000	300	48.55%	0.5730	0.6033	0.2626	0.3771	0.2611	0.1941	34.98
	600		48.42%	0.5703	0.6055	0.2633	0.3912	0.2620	0.1958	34.09
OPEN	-	-	47.46%	0.5606	0.6239	0.2661	0.3952	0.2826	0.1992	29.42
	12000	300	51.80%	0.6043	0.5314	0.2679	0.3457	0.2095	0.1922	46.39
	600		51.57%	0.6019	0.5368	0.2726	0.3493	0.2102	0.1905	28.99
			51.48%	0.6014	0.5389	0.2727	0.3460	0.2088	0.1939	26.31
			50.24%	0.5922	0.5542	0.2732	0.3524	0.2144	0.1959	25.97

Table 11. Results of pruning queries. We use StreamPETR-vov-1600x640 and OPEN-r101-1408x512.

r	mAP \uparrow	NDS \uparrow	mATE \downarrow	mASE \downarrow	mAOE \downarrow	mAVE \downarrow	mAAE \downarrow
-	43.07%	0.5389	0.6023	0.2686	0.4238	0.2597	0.2105
2000	42.99%	0.5382	0.6035	0.2696	0.4230	0.2609	0.2099

Table 12. Pruning fully converged models. We train StreamPETR-r50-704x256 for 120 epochs to ensure its full convergence. The first line remaining r blank is the original model’s results without pruning.

704x256 with $n=4$ in Tab. 10. We believe this is related to the redundant information in the image features. As shown in Fig. 8, the key is the image feature extracted by the backbone, which inevitably contains background information (such as sky, buildings, etc.) that is ineffective for object detection. These keys interact with the query and affect the detection performance.

In the original 3D detectors, for each transformer decoder layer, the query is continuously updated, while the key and value remain unchanged. Therefore, the background key repeatedly influences the query. In fact, it can be argued that the “unimportant keys” pruned by our method are essentially background tokens. It is precisely because these keys, which interfere with detection, are pruned that the phenomenon of increased model performance occurs.

D.2. Pruning Queries

While it is possible to prune both keys and queries at runtime, the latter’s involvement in self-attention operations limits the extent of pruning. To ensure that the mAP degradation does not exceed 1%, we cannot prune 300 queries, offering only marginal speed improvements. Conversely, to achieve significant acceleration in model speed, pruning 600 queries would result in a sharp decline in mAP. The results are shown in Tab. 11.

We believe that pruning the key is more effective than pruning the query for the following reasons: The key does not have explicit self-attention. In contrast, after interacting with the key, the query is fed into the self-attention mechanism of the next layer. This introduces internal dependencies, meaning that even if a query generates a low classification score, its value may influence queries with high clas-

r	mAP \uparrow	NDS \uparrow	mATE \downarrow	mASE \downarrow	mAOE \downarrow	mAVE \downarrow	mAAE \downarrow	Training Time
-	48.89%	0.5732	0.6096	0.2601	0.3882	0.2603	0.1944	2d 14h
21000	49.42%	0.5787	0.5982	0.2579	0.3651	0.2698	0.1926	2d 13h

Table 13. Training StreamPETR-vov-1600x640 with tgGBC, while tgGBC is applied, n and k are set to 1 and 175, respectively.

sification scores through self-attention. Therefore, pruning the query can have a significant impact on the remaining queries, thereby degrading model performance. In contrast, the dependencies of the key are indirect, so pruning the key has a lower impact on model performance. Moreover, keys contain redundant information more than queries. Please see the analysis in Appendix D.1.

D.3. Pruning Fully Converged Models

To ensure a fair comparison with prior work while considering training efficiency, many previous experiments use a 24-epoch training schedule, which often does not achieve full convergence. To assess whether tgGBC remains effective after full convergence, we trained a StreamPETR-ResNet50-704x256 model for 120 epochs. As shown in Tab. 12, tgGBC preserves the model’s performance even after full convergence, with only a 0.08% decrease in mAP and a 0.0007 reduction in NDS.

D.4. Training with tgGBC

If there is a new model, one can also train it with tgGBC from the beginning, as shown in Tab. 13. Our method is capable of reducing training time. For example, training StreamPETR-vov-1600x640 with $r = 21000$ and $n = 1$ for 30 epochs takes less time than training without tgGBC for 24 epochs while achieving a better mAP.

D.5. 2D Object Detection Models with tgGBC

As described in Sec. 2.2, the number of keys in ViT-based methods is significantly smaller than that in 3D object detection methods. Similarly, the number of keys in 2D object detection is around 1,000 (e.g., in ConditionalDETR). This is also why we focus on 3D object detection rather than extensively studying 2D object detection methods. Moreover,

Model	Backbone	TgGBC	mAP \uparrow	AP ₅₀ \uparrow	AP ₇₅ \uparrow	AP _s \uparrow	AP _m \uparrow	AP ₁ \uparrow	Inf. Time (ms) \downarrow
DETR	ResNet50	-	0.421	0.623	0.442	0.214	0.460	0.610	42.06
		✓	0.414	0.620	0.436	0.205	0.455	0.603	35.24 (-16.21%, 1.19x)
ConditionalDETR	ResNet101	-	0.435	0.638	0.463	0.218	0.480	0.480	54.61
		✓	0.426	0.635	0.453	0.211	0.470	0.608	47.01 (-13.92%, 1.16x)
ConditionalDETR	ResNet50	-	0.409	0.619	0.434	0.207	0.442	0.595	43.88
		✓	0.400	0.615	0.427	0.196	0.436	0.587	40.13 (-8.55%, 1.09x)
ConditionalDETR	ResNet101	-	0.428	0.636	0.459	0.218	0.467	0.610	69.97
		✓	0.424	0.635	0.454	0.215	0.463	0.605	55.66 (-20.45%, 1.26x)

Table 14. Results of DETR and ConditionalDETR with tgGBC. Lines with “tgGBC” remaining blank are the original results without pruning.

current 2D object detection methods are rapidly evolving and highly mature. Methods based on DETR are not the absolute mainstream, as other approaches, such as the YOLO series, are still widely used in 2D object detection tasks.

Additionally, 3D object detection is a highly practical and valuable task. Therefore, from the very beginning, we focused on pruning 3D object detection models. However, for some DETR-based 2D detection methods, tgGBC can still be applied. Here, we take ConditionalDETR as an example to verify the effectiveness of tgGBC on 2D object detection methods, as shown in Tab. 14.

In ConditionalDETR, the number of keys is not always the same. Therefore, we adopt a configuration similar to MV2D, using r to represent the pruning ratio and set a threshold t . When the current number of keys exceeds t , pruning is performed. Through experiments, tgGBC can reduce the model’s inference time by 19.17% (1.24 \times) while keeping the mAP degradation below 1%.